Physics Open 28 (2026) 100446

Contents lists available at ScienceDirect

Physics Open

journal homepage: www.sciencedirect.com/journal/physics-open

GST-based optical switch using dual stub metal-insulator-metal structure with low switching energy and improved functionality for neuromorphic applications

Ozra Sharifipour, Parviz Keshavarzi, Mohammad Danaie *

Faculty of Electrical and Computer Engineering, Semnan University, Semnan, Iran

ARTICLE INFO

Keywords:
Optical switch
Phase-change material
Plasmonic resonator
Neuromorphic photonics
$Ge_2Sb_2Te_5$ (GST)
Metal–Insulator–Metal (MIM)

ABSTRACT

A compact plasmonic optical switch based on a dual-stub metal–insulator–metal (MIM) filtering structure is proposed for neuromorphic photonic applications. Switching functionality is achieved by integrating a nanoscale $Ge_2Sb_2Te_5$ (GST) phase-change layer with dimensions of 35×10 nm^2 into the resonator coupling region. Numerical simulations demonstrate that the proposed device operates with an estimated absorbed switching energy of approximately 4 pJ in the GST region, representing a significant reduction compared with representative Kerr-based plasmonic switches reported in the literature. Owing to the optimized resonator geometry and precise nanoscale engineering of the GST layer, a high switching contrast of up to 87% is achieved while maintaining an ultra-compact footprint of 0.035 μm^2. In addition, the non-volatile nature of GST enables stable optical transmission states and provides a promising physical platform for programmable optical synaptic devices in future neuromorphic photonic systems. The obtained results highlight the potential of GST-assisted plasmonic switches as low-energy, compact, and scalable building blocks for next-generation neuromorphic photonic networks.

1. Introduction

The rapid growth of data-intensive applications has created an increasing demand for computing and communication platforms that simultaneously provide high processing speed, low energy consumption, and large-scale integration capability [1–3]. Conventional electronic systems, which rely on charge transport mechanisms, face fundamental limitations including excessive power dissipation, thermal management challenges, and restricted bandwidth, which ultimately constrain scalability and computational efficiency [3–6].

Photonic technologies have emerged as a promising alternative by utilizing photons as information carriers, enabling high-speed signal transmission with significantly reduced energy dissipation [7]. Owing to their immunity to electromagnetic interference and inherent parallelism in multi-wavelength operation, photonic systems enable high-bandwidth, low-latency data transfer and are therefore strong candidates for next-generation computing paradigms, including neuromorphic computing and artificial intelligence [8–14].

Neuromorphic computing aims to emulate biological neural systems through distributed and massively parallel architectures capable of energy-efficient information processing [15–18]. In photonic neuromorphic hardware, the realization of compact, programmable, and non-volatile optical synapses is a critical requirement [19,20]. Despite significant progress in CMOS-based implementations, challenges related to power consumption, scalability, and thermal limitations remain unresolved [21–25], motivating the exploration of photonic and plasmonic alternatives.

Plasmonic structures offer a viable route to overcome these limitations by enabling subwavelength optical confinement through surface plasmon polaritons (SPPs) at metal–dielectric interfaces [26–28]. This strong confinement enhances light–matter interaction and enables ultra-compact photonic devices, which have been widely investigated for applications in integrated photonics, sensing, and neuromorphic computing [29–34].

A large number of reported plasmonic switches are based on Kerr nonlinearity, where refractive index modulation is governed by optical intensity [35–37]. Although such mechanisms enable ultrafast response, their inherently volatile nature prevents stable state retention, which is essential for synaptic functionality. Moreover, the relatively weak nonlinear coefficients of practical materials often require high optical intensities, leading to increased energy consumption [38–40].

In contrast, phase-change materials (PCMs), particularly $Ge_2Sb_2Te_5$

* Corresponding author.
E-mail address: danaie@semnan.ac.ir (M. Danaie).

https://doi.org/10.1016/j.physo.2026.100446
Received 17 December 2025; Received in revised form 27 June 2026; Accepted 6 July 2026
Available online 8 July 2026

(GST), provide an effective route toward non-volatile optical switching [41–43]. GST exhibits reversible transitions between amorphous and crystalline phases, accompanied by large and persistent changes in optical constants [44–46]. These states can be retained without continuous power supply, enabling intrinsic memory functionality. Phase transitions can be triggered by optical pulses with moderate energy, while the large refractive index contrast between phases enables strong optical modulation within compact footprints [47–49].

However, most existing GST-based plasmonic switches are still limited by conventional geometries that restrict field confinement and device scaling [50–52]. To address these limitations, this work proposes a co-designed dual-stub metal–insulator–metal (MIM) plasmonic resonator incorporating a nanoscale GST element positioned at the electromagnetic hotspot [53–55]. This hotspot-engineered configuration enhances near-field coupling and strengthens light–matter interaction, leading to improved modulation efficiency [56–58]. The device geometry is systematically optimized to maximize the transmission contrast at the selected operating wavelength, which is used consistently throughout the subsequent analyses.

Coupled electromagnetic and transient thermal simulations demonstrate binary non-volatile optical switching with a switching contrast of up to 87% and an estimated absorbed switching energy of approximately 4 pJ in the GST region, while maintaining an ultra-compact footprint of 0.035 μm^2. The switching process is governed by thermally induced phase transitions in GST, resulting in a switching time of approximately 50–200 ns. Although this response is slower than Kerr-based ultrafast mechanisms, it is fully compatible with neuromorphic photonic applications, where memory retention and energy efficiency are primary requirements.

Collectively, these characteristics demonstrate that the proposed GST-assisted plasmonic switch constitutes a promising building block for compact, energy-efficient, and non-volatile optical synapses in future integrated neuromorphic photonic systems.

2. Comparative analysis of Kerr nonlinearity and phase-change materials for plasmonic optical switching in neuromorphic architectures

The realization of neuromorphic photonic systems requires optical switching mechanisms that simultaneously satisfy compact footprint, low-energy operation, high modulation depth, and stable state retention. In plasmonic architectures, the underlying switching mechanism critically influences the energy efficiency, operational stability, and the potential implementation of optical synaptic functionality in neuromorphic architectures [59–61]. Among the most widely investigated approaches, Kerr nonlinearity and phase-change materials (PCMs) represent two fundamentally distinct physical mechanisms for optical modulation [61–63].

Kerr nonlinearity originates from the third-order nonlinear optical response, where the refractive index varies proportionally with optical intensity [64–67]. In metal–insulator–metal (MIM) plasmonic structures, strong field confinement enhances this effect, enabling intensity-dependent refractive index modulation expressed as [68,69]:

$$n(I) = n_0 + n_2 I \tag{1}$$

where n_0 is the linear refractive index, n_2 the nonlinear Kerr coefficient, and I the optical intensity. The induced phase change $\Delta\phi$ over a device length L at wavelength λ is given by:

$$\Delta\varphi = \frac{2\pi}{\lambda}\Delta n \cdot L \tag{2}$$

Kerr-based switches exhibit femtosecond-scale response due to the instantaneous electronic origin of the nonlinearity. However, this response is inherently volatile, since the refractive index immediately returns to its initial state after removal of optical excitation [70–72]. Moreover, the weak nonlinear coefficient in practical materials requires high optical intensities, leading to increased energy consumption and optical losses [73,74].

In contrast, phase-change materials such as $Ge_2Sb_2Te_5$ (GST) enable non-volatile optical switching through reversible structural transitions between amorphous and crystalline phases [75–78]. These transitions induce large and persistent variations in both refractive index and extinction coefficient, enabling stable optical state retention without continuous energy input [79].

The phase-transition dynamics are governed by transient heat diffusion processes [80,81].

$$\rho c_p \frac{\partial T}{\partial t} = \nabla.(\kappa \nabla T) + Q \tag{3}$$

where ρ is density, c_p is specific heat capacity, κ is thermal conductivity, T is temperature, and Q is absorbed optical power density.

In the proposed plasmonic architecture, the switching process follows a sequential physical pathway. Initially, the TM-polarized guided mode propagates through the MIM waveguide. This excitation generates surface plasmon polaritons (SPPs), which are strongly confined within the dual-stub resonator region [82–84].

The dual-stub geometry leads to hybridized resonant modes and enhances electromagnetic field localization in the active region. Consequently, a strong optical hotspot is formed at the GST nanoregion, resulting in a maximum absorbed optical power density Q.

The localized optical energy is converted into heat, increasing the temperature of the GST layer. When the temperature exceeds the phase-transition thresholds, GST undergoes a reversible transition between amorphous and crystalline states [85–87]. This phase change modifies the complex permittivity, leading to a variation in the effective modal index n_{eff}.

Throughout this work, the ON state is defined as the high-transmission state of the device, whereas the OFF state corresponds to the low-transmission state. The transition from the crystalline to the amorphous phase (RESET process) and the reverse transition from the amorphous to the crystalline phase (SET process) modify the optical transmission through changes in the complex refractive index of GST. Depending on the selected operating wavelength, either the amorphous or crystalline phase may correspond to the ON or OFF state due to the wavelength-dependent resonance characteristics of the proposed device. These definitions are used consistently throughout the manuscript. Importantly, this switching mechanism is not solely governed by the intrinsic properties of GST, but results from the combined effect of resonator mode hybridization, electromagnetic hotspot engineering, and the integration of the GST phase-change nanoregion. A key advantage of GST is multi-level programmability via partial crystallization. The effective refractive index is expressed as [88]:

$$n_{eff}(p) = (1-p)n_a + p n_c \tag{4}$$

where n_a and n_c are the refractive indices of the amorphous and crystalline phases, respectively. The optical transmission through a GST layer of thickness d and extinction coefficient κ follows:

$$T = exp(-\alpha d) = exp\left(-\frac{4\pi\kappa}{\lambda}d\right) \tag{5}$$

These relations establish the physical basis for non-volatile multi-level synaptic weight control through partial crystallization. Although the present work demonstrates binary optical switching, the same physical mechanism can be extended to multi-level operation in future implementations.

A qualitative comparison is summarized in Table 1. Kerr nonlinearity provides ultrafast femtosecond modulation driven by instantaneous third-order effects. However, its volatile nature, limited modulation depth, and high optical power requirement restrict its applicability in neuromorphic systems requiring memory functionality.

Table 1
Comparative analysis of Kerr nonlinearity- and GST-based plasmonic switching mechanisms in terms of their physical operating principles, switching dynamics, optical memory characteristics, energy consumption, and suitability for neuromorphic photonic applications. The comparison highlights the fundamental trade-off between ultrafast volatile Kerr switching and non-volatile thermo-optical phase-change switching based on GST.

Feature	Kerr nonlinearity	GST-based switching
Physical origin	Instantaneous third-order optical nonlinearity	Thermally driven, reversible phase-change process
Response/switching time	Femtosecond-scale	Sub-microsecond to hundreds-of-nanoseconds (optical-pulse dependent)
Volatility	Volatile	Non-volatile
State retention	Not supported	Supported
Modulation depth	Limited	High
Power/write energy	High optical intensity required	Lower update energy for nanoscale cells
Potentially supported via partial crystallization	Limited	Supported via partial crystallization
Neuromorphic relevance	Suitable for ultrafast modulation, not memory	Suitable for synaptic storage and memory-like operation

In contrast, GST-based switching is governed by thermo-optical phase transitions. Although switching time is longer (nanoseconds to sub-microseconds depending on geometry and pulse conditions), it provides essential non-volatility and state retention. Importantly, this time scale is fully compatible with neuromorphic computing requirements, where synaptic update rates are significantly lower than optical carrier dynamics.

Unlike conventional GST-based plasmonic switches relying on single-resonator configurations, the proposed design exploits a dual-stub MIM resonator supporting hybridized symmetric and antisymmetric modes. This configuration significantly enhances field confinement and increases sensitivity to nanoscale refractive index perturbations induced by GST phase transitions, leading to improved modulation efficiency and extinction ratio within an ultra-compact footprint.

Although GST exhibits moderate optical loss compared to low-loss PCMs such as Sb_2S_3 and Sb_2Se_3, it offers significantly higher refractive index contrast and mature experimentally validated switching dynamics. A comparative overview is presented in Table 2.

Overall, while low-loss materials reduce absorption, GST provides a more favorable trade-off between modulation depth, fabrication maturity, and reliable nanoscale switching behavior.

In this work, the proposed device adopts a previously reported Kerr-based dual-stub MIM geometry; however, the physical switching mechanism is fundamentally redefined. Instead of instantaneous Kerr-induced refractive index modulation, the nonlinear medium is replaced with a nanoscale GST element positioned at the electromagnetic hotspot. This transformation enables a transition from a volatile intensity-driven response to a non-volatile thermo-plasmonic switching mechanism, while preserving the original geometric advantages and significantly enhancing memory functionality and modulation depth.

Overall, although low-loss phase-change materials may offer reduced optical absorption, GST remains a balanced and practically favorable choice for the proposed device due to its large refractive index contrast, non-volatile operation, mature fabrication compatibility, and reliable nanoscale switching behavior. These characteristics make GST particularly suitable for compact, low-power photonic switching devices that can serve as building blocks for programmable optical synapses in neuromorphic photonic architectures, enabling efficient optical signal modulation and providing the physical basis for future neuromorphic information processing [90].

Based on the comparative analysis presented above, the proposed work adopts the dual-stub MIM architectural framework of Kerr-based plasmonic switches; however, the underlying physical modulation mechanism is fundamentally redefined [91]. Instead of relying on instantaneous Kerr-induced refractive index modulation, the nonlinear medium is replaced by a phase-change material (GST) positioned at the electromagnetic hotspot, enabling a transition from a volatile intensity-dependent response to a non-volatile thermo-plasmonic switching mechanism. This substitution preserves the geometrical advantages of the reference structure while introducing memory functionality, enhanced modulation depth, and a bistable optical response essential for neuromorphic photonic applications [92,93].

3. Design methodology and electromagnetic modeling of the proposed GST-based plasmonic switch

This section first reviews the Kerr-nonlinearity-based plasmonic switch reported in the reference study to establish a physically consistent baseline for comparison. The proposed GST-integrated dual-stub MIM switch is subsequently introduced, and its electromagnetic design principles, numerical implementation, and structural optimization are described in detail. This organization enables a direct assessment of the effect of replacing the volatile Kerr nonlinear medium with a non-volatile phase-change material while preserving a comparable plasmonic resonator architecture.

3.1. Review of the plasmonic switch structure based on Kerr nonlinearity in the reference article

In this section, previously reported Kerr-based plasmonic switch, designed based on exploiting the Kerr nonlinear effect, is thoroughly examined.

The structure consists of a metal–insulator–metal (MIM) waveguide with a width of w = 50 nm, equipped with two identical parallel stub resonators having both width and length equal to that of the waveguide (i.e., width w = 50 nm and length Ls = 500 nm). The distance between the two stubs is set at d = 420 nm. A Kerr-type nonlinear material fills the region between and inside the stubs, whose nonlinear refractive index is actively controlled by the intensity of an external optical pump.

The geometric parameters of the structure are chosen such that the widths of both the waveguide and the stubs are 50 nm, and the stub length is 500 nm. To achieve ultrafast switching, metal–insulator composite materials with strong third-order nonlinear susceptibility and femtosecond-scale response times are employed. Specifically, the Kerr nonlinear material is selected as an Au:SiO_2 composite with a linear refractive index of n_0 = 1.47 and a Kerr coefficient of n_2 = 2.07×10−1 μm2/W and exhibits femtosecond-scale response times. The variation of the nonlinear refractive index as a function of

Table 2
Comparative overview of representative phase-change materials for neuromorphic plasmonic switching in terms of their optical properties, switching performance, non-volatility, and suitability for photonic synaptic applications. The comparison highlights the characteristics that motivate the selection of GST as the active material in the proposed plasmonic switch.

Material	Refractive Index Contrast	Optical Loss	Switching Energy	Fabrication Maturity	References
GST ($Ge_2Sb_2Te_5$)	High	Moderate	Low	High	[61–64,89]
Sb_2S_3	Moderate	Very Low	Comparable	Moderate	[90–92]
Sb_2Se_3	Moderate	Very Low	Comparable	Moderate	[93–95]

pump intensity I is defined according to formula (2) in the reference article.

It is noteworthy that the schematic of the plasmonic switch structure, along with transmission spectral responses and electric field distributions presented in Figs. 1 and 2, are derived and redrawn based on the results of the reference article. They are utilized here to maintain coherence and allow better comparison with the optimized structure proposed in this study. Fig. 1 illustrates the schematic of the plasmonic switch structure with two parallel stub resonators and the Kerr material located in the gap between them.

Fig. 2 depicts the transmission spectra of the MIM waveguide under two different pump intensities. Results show that increasing the pump intensity to 145 mW/μm^2 causes the Fano resonance peak to red-shift from 1485 nm to 1520 nm, while transmission at 1485 nm simultaneously decreases from 0.53 to 0.03. Accordingly, the signal wavelength for the switching operation is set at 1485 nm.

3.2. Design and analysis of the proposed plasmonic switch structure incorporating a GST element: geometrical and structural specifications

The proposed plasmonic switch is based on a metal–insulator–metal (MIM) configuration engineered to achieve an ultra-compact footprint, strong electromagnetic confinement, and efficient phase-change-based optical modulation. The architecture is optimized to maximize light–matter interaction within a nanoscale $Ge_2Sb_2Te_5$ (GST) active region, enabling non-volatile, low-energy switching suitable for neuromorphic photonic applications. This section focuses on the electromagnetic design principles, numerical modeling framework, geometrical optimization, and material implementation to ensure reproducibility and physical consistency.

Although the proposed device is conceptually inspired by the previously reported dual-stub plasmonic switch, the present design is not obtained by simply replacing the Kerr nonlinear medium with GST. Instead, the resonator geometry, including the stub dimensions, inter-stub separation, and the placement of the GST active region, is systematically re-optimized to maximize electromagnetic field confinement, resonance modulation, and thermo-optical switching efficiency. Consequently, the performance improvements reported in this work arise from the combined optimization of the plasmonic resonator and the phase-change material rather than from material substitution alone.

All electromagnetic simulations are performed using the two-dimensional finite-difference time-domain (2D-FDTD) method implemented in Lumerical FDTD Solutions. The numerical parameters, including boundary conditions, mesh refinement, and simulation time, are selected to ensure numerical convergence and eliminate discretization-induced variations in the calculated transmission spectra.

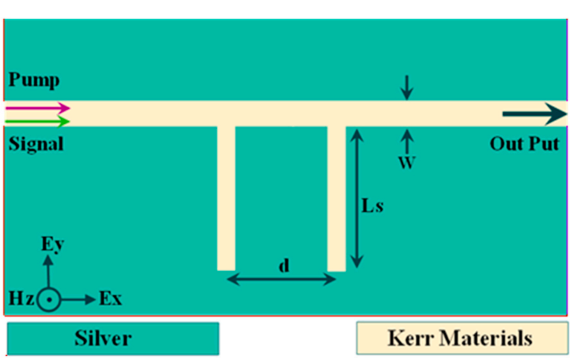

Fig. 1. Schematic illustration of the reference metal–insulator–metal (MIM) plasmonic switch employing two identical parallel stub resonators with a Kerr nonlinear Au:SiO_2 composite filling the coupling region. The structure is presented as the baseline architecture for comparison with the proposed GST-based plasmonic switch, illustrating the original Kerr-based switching mechanism and device configuration. (Adapted from Ref. [53]).

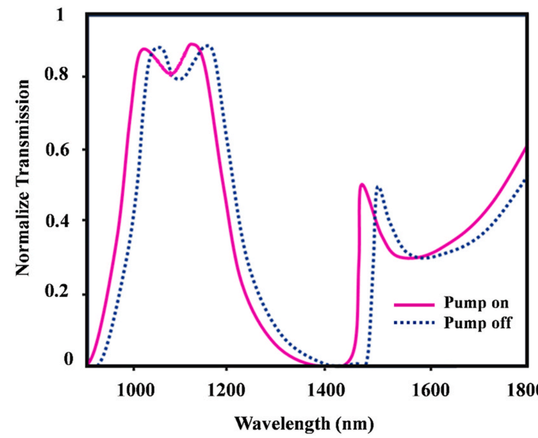

Fig. 2. Transmission spectra of the dual-stub MIM plasmonic switch under two optical pump intensities. The structural parameters are waveguide and stub width w = 50 nm, stub length L_s = 500 nm, and stub separation d = 420 nm. The blue solid curve corresponds to the unpumped state (I = 0), whereas the red dash–dot curve represents the pumped state (I = 145 mW/μm^2). Optical pumping induces a resonance redshift from approximately 1485 nm to 1520 nm, accompanied by a significant reduction in transmission at the operating wavelength, illustrating the Kerr-nonlinearity-based switching mechanism. (Adapted from Ref. [53]).

This approach is widely adopted in plasmonic and nanophotonic devices due to its capability to accurately resolve subwavelength field confinement and dispersive material responses. The 2D formulation is justified by the translational invariance of the structure along the out-of-plane direction and the dominant excitation of transverse magnetic (TM) surface plasmon polariton (SPP) modes in MIM waveguides, where out-of-plane field variation is negligible.

Perfectly matched layer (PML) boundary conditions are applied along both x- and y-directions to eliminate artificial reflections. A fundamental TM-polarized mode source is used to excite the SPP modes in the MIM waveguide. To accurately capture nanoscale hotspots and steep field gradients near the GST region, a non-uniform adaptive mesh with a minimum grid size of 1 nm is employed.

A systematic mesh convergence study is performed to ensure that transmission spectra, resonance wavelengths, and field enhancement factors remain invariant under further mesh refinement. The simulation time window and frequency-domain monitors are carefully optimized to guarantee steady-state convergence and accurate extraction of spectral response. The final mesh size represents a compromise between computational efficiency and numerical accuracy.

The dispersive optical properties of silver (Ag) are modeled using the experimentally validated Johnson–Christy model, while GST is implemented as a phase-dependent dispersive material using experimentally measured wavelength-dependent complex refractive index data (n and k) from Ref. [94]. No fitting or artificial modification of the experimental optical constants is introduced. The significant difference between amorphous and crystalline phases directly affects absorption, effective refractive index, and resonance conditions. In particular, the crystalline phase exhibits higher refractive index and extinction coefficient, resulting in stronger attenuation and enhanced perturbation of plasmonic resonances.

Fig. 3 presents the optimized GST-integrated dual-stub plasmonic switch. The two-dimensional geometry shown in Fig. 3(a) is employed in all electromagnetic simulations, whereas the three-dimensional rendering in Fig. 3(b) is included solely to facilitate physical visualization of the device architecture.

The structure consists of a MIM waveguide integrated with two parallel stub resonators. The waveguide width is w_1 = 50 nm, each stub has length l = 500 nm and width w_2 = 20 nm, and the separation between stubs is d = 50 nm. A GST nanostructure with dimensions

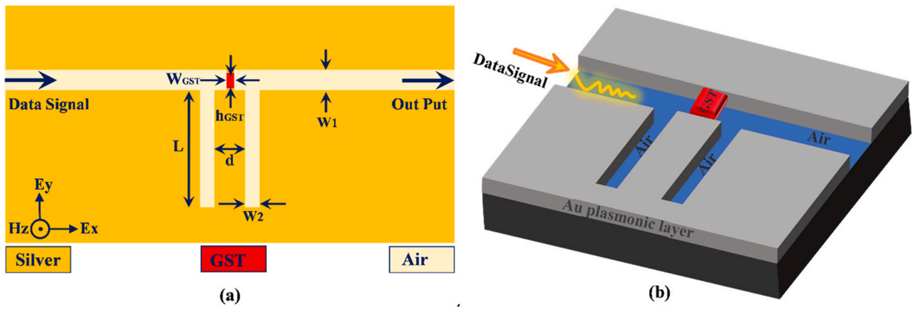

Fig. 3. Schematic of the proposed dual-stub MIM plasmonic switch incorporating a nanoscale GST active region. (a) Two-dimensional geometry employed for the electromagnetic simulations, consisting of a MIM waveguide and two parallel stub resonators with w = 50 nm, L_s = 500 nm, and d = 50 nm. (b) Three-dimensional representation provided for physical visualization of the device architecture. The GST element is intentionally positioned at the electromagnetic coupling hotspot, where the electric-field intensity is maximized to enhance plasmon–GST interaction and improve switching efficiency.

35×10 nm^2 is positioned at the central coupling hotspot where electromagnetic energy density is maximized. These dimensions are determined through the systematic optimization presented in Section 4. The dual-stub configuration supports strong near-field coupling mediated by SPP propagation, leading to hybridized resonant modes (symmetric and antisymmetric states). This mode hybridization produces sharp spectral features and enhances sensitivity to refractive index variations induced by GST phase transitions.

Physically, the system behaves as a plasmonic Fabry–Pérot-like cavity, where multiple reflections between stub resonators create standing-wave conditions. This results in strong field confinement and increased local density of optical states (LDOS) at resonance. The stub resonance condition can be approximated as:

$$L \approx m\left(\frac{\lambda_{SPP}}{2n_{\mathrm{eff}}}\right) \tag{6}$$

where λ_{SPP} is the surface plasmon polariton wavelength, n_{eff} is the effective modal index, and m is an integer mode number. The switching operation is governed by optical excitation of TM modes in the MIM waveguide. The GST element is intentionally positioned at the electromagnetic hotspot, where the local electric-field intensity reaches its maximum value, thereby maximizing the interaction between the confined plasmonic mode and the phase-change material. The resulting strong SPP confinement enhances the absorbed optical power density Q, which initiates the thermo-optical phase transition while reducing the switching energy required for device operation.

The dual-stub configuration enables strong near-field coupling through SPP propagation in the MIM waveguide, creating a highly localized electromagnetic hotspot at the coupling region. The GST nanostructure is intentionally positioned at this hotspot, where the local electric-field intensity reaches its maximum value, thereby maximizing the interaction between the confined plasmonic mode and the phase-change material while minimizing the optical energy required to trigger the phase transition. This resonant-field engineering constitutes the primary design strategy of the proposed device and forms the physical basis for the thermo-optical switching mechanism analyzed in the following section.

3.3. *Thermo-optical switching mechanism and comprehensive thermal model validation*

Throughout this work, the amorphous GST state is defined as the ON state with high optical transmission, whereas the crystalline GST state corresponds to the OFF state with low transmission. Accordingly, the RESET operation produces the amorphous state, while the SET operation restores the crystalline state. This terminology is used consistently throughout the manuscript.

The thermo-optical switching mechanism of the proposed plasmonic device originates from photothermal conversion induced by the strong plasmonic field confinement within the nanoscale GST active region. To accurately describe the switching process, the electromagnetic response presented in Section 3.2 is coupled with a transient thermal model, enabling a self-consistent multiphysics analysis of optical absorption, heat generation, and phase-transition dynamics.

Switching between the two non-volatile optical states is governed by reversible phase transitions of the GST layer. During the SET process, a moderate-intensity optical pulse with a relatively long duration increases the GST temperature above the crystallization threshold (~413 K) while remaining below the melting temperature (~870 K), thereby inducing crystallization. Conversely, the RESET process is achieved by applying a short, high-intensity optical pulse that raises the GST temperature above its melting point, followed by rapid cooling that produces the amorphous phase. This thermo-optical mechanism provides deterministic, repeatable, and non-volatile switching behavior. The volumetric optical power converted into heat is expressed as:

$$Q = \frac{1}{2}\omega\varepsilon_0\varepsilon''|E|^2 \tag{7}$$

where ε'' is the imaginary part of GST's permittivity and depends on its phase. Localized heating is modeled using the transient heat conduction equation:

$$\rho c_p\frac{\partial T}{\partial t} = \nabla.(\kappa\nabla T) + Q \tag{8}$$

where ρ, c_p, and k represent density, specific heat capacity, and thermal conductivity, respectively. To maintain consistency with the electromagnetic simulations, all thermal calculations are performed using the same two-dimensional computational framework. This approximation is justified by the translational invariance of the MIM structure together with the predominance of in-plane heat diffusion in the proposed nanoscale geometry. The optical constants of GST are directly taken from experimentally measured wavelength-dependent data reported in Ref. [94] and implemented in the FDTD simulations to accurately represent the phase-dependent optical response.

Electromagnetic propagation is described by the Helmholtz equation:

$$\nabla^2 E + \kappa_0{}^2 n_{eff}{}^2 E = 0 \tag{9}$$

where $\kappa_0 = \frac{2\pi}{\lambda}$ and n_{eff} depends on the crystallization state of GST. Resonant behavior follows a Lorentzian response:

$$\mathscr{F}(E; E_{res}, \Gamma) = \frac{\left(\Gamma/2\right)^2}{(E - E_{res})^2 + \left(\Gamma/2\right)^2} \tag{10}$$

Fig. 4 presents the normalized transmission spectra corresponding to

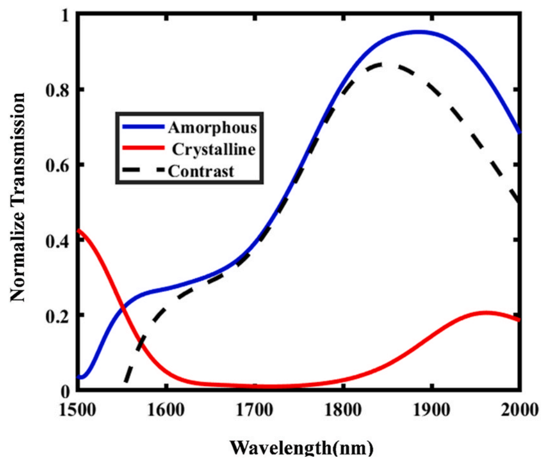

Fig. 4. Normalized transmission spectra of the proposed GST-based dual-stub plasmonic switch for the two stable phase states of the GST active region. The amorphous phase (blue curve) exhibits a transmission exceeding 90%, corresponding to the ON state, whereas the crystalline phase (red curve) suppresses the transmission to below 5%, corresponding to the OFF state. The resulting transmission contrast (black curve) exceeds 87%, demonstrating efficient modulation arising from the phase-dependent optical properties of GST and confirming strong optical state discrimination suitable for non-volatile neuromorphic photonic applications.

the amorphous and crystalline GST phases. At the selected operating wavelength of the proposed device, the amorphous phase exhibits a transmission exceeding 90% and therefore corresponds to the ON state, whereas the crystalline phase exhibits a transmission below 5% and represents the OFF state.

The resulting transmission contrast exceeds 87%, demonstrating excellent optical state discrimination suitable for neuromorphic photonic applications. These ON/OFF definitions are used consistently throughout the manuscript. The transmission contrast is defined as:

$$Contrast = T_{on} - T_{off} \tag{11}$$

which exceeds 87% for the optimized device geometry [95–98]. The transmission dependence on GST absorption can be approximated by:

$$T \propto e^{-4\pi kd} \tag{12a}$$

The corresponding electromagnetic field distributions are shown in Fig. 5. In the amorphous phase, strong field localization ($|E|^2 > 1.6$) is observed inside the GST region, indicating efficient plasmon–GST coupling and enhanced optical confinement. After crystallization, the increased absorption and modified complex refractive index weaken the field confinement and reduce the transmitted intensity [99]. These results confirm that optical switching originates from the phase-dependent redistribution of the confined electromagnetic field rather than from material absorption alone [100–102].

Fig. 6 illustrates the simulated temperature distributions during the switching process. During RESET operation, the GST temperature reaches approximately 950 K, exceeding the melting temperature and enabling melting followed by rapid quenching into the amorphous phase. During SET operation, the temperature stabilizes around 470 K, remaining above the crystallization threshold while below the melting temperature, thereby enabling controlled crystallization.

At the nanoscale, thermal transport across the GST–silver interface is influenced by Kapitza thermal resistance arising from phonon mismatch [103,104]. Instead of explicitly modeling atomistic interface transport,

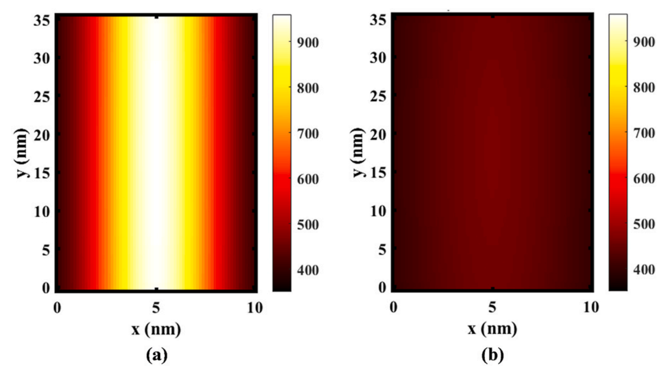

Fig. 6. Simulated temperature distribution in the GST active region under optical excitation. (a) During the RESET process (amorphization), the temperature reaches approximately 950 K, exceeding the GST melting temperature and enabling melting followed by rapid quenching. (b) During the SET process (crystallization), the temperature stabilizes at approximately 470 K, remaining above the crystallization temperature while below the melting point, thereby enabling controlled crystallization. The temperature profiles demonstrate highly localized photothermal heating within the GST active region, supporting efficient thermo-plasmonic switching under the adopted two-dimensional simulation framework.

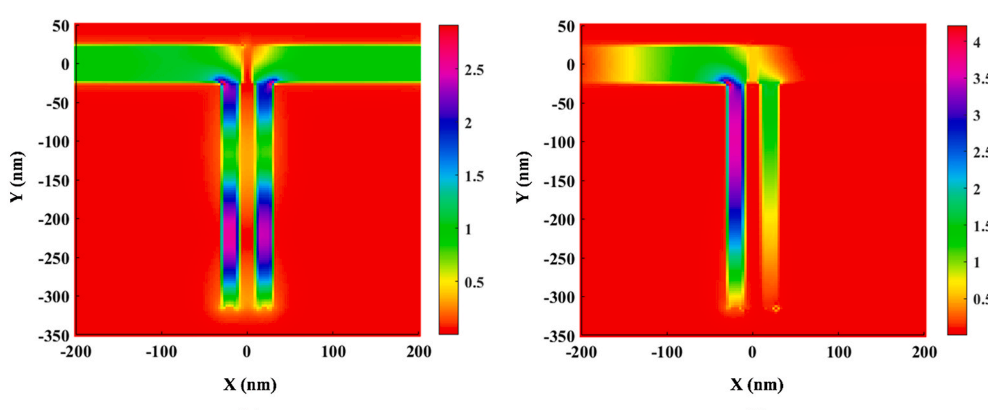

Fig. 5. Normalized electric-field magnitude (|E|) distribution in the proposed GST-based dual-stub plasmonic switch for the two stable phase states of the GST active region. (a) In the amorphous state, strong electromagnetic field localization is observed at the GST hotspot, indicating efficient plasmon–GST coupling and enhanced light–matter interaction, which promotes localized optical absorption for thermo-optical switching. (b) In the crystalline state, the increased refractive index and optical absorption of GST modify the resonant field distribution, resulting in weaker field confinement and reduced transmitted intensity. The pronounced phase-dependent redistribution of the electromagnetic field confirms that optical modulation is governed by the perturbation of the localized plasmonic resonance induced by the GST phase transition.

this effect is incorporated through an effective thermal coupling approximation, which is widely adopted in nanoscale opto-thermal simulations and provides a computationally efficient yet physically realistic description. Owing to the high thermal conductivity of silver, heat dissipation is dominated by lateral heat spreading, effectively suppressing excessive thermal accumulation within the GST region [105–108].

The thermophysical parameters used in the transient thermal simulations are summarized in Table 3. Temperature dependence of the material properties is neglected because of the short optical pulse duration and the extremely small thermal volume, which represents a commonly adopted approximation in phase-change nanophotonics [109,110].

Optical excitation is introduced through a TM-polarized guided mode operating at the selected resonance wavelength of the optimized plasmonic switch. Gaussian optical pulses with full-width at half-maximum (FWHM) values of 100 ns for the SET operation and 10 ns for the RESET operation are employed. The corresponding pulse powers are selected to satisfy the thermal requirements for crystallization and amorphization while maintaining switching energies in the picojoule range.

The switching energy is defined as:

$$E_{switch} = \int_0^{t_p} \int_V Q(r,t)dVdt \tag{12b}$$

while the required thermal energy is estimated as:

$$E_{thermal} = \rho V c_p \Delta T + \rho V L \tag{13}$$

where L is the latent heat of phase transition.

Since both the electromagnetic and thermal simulations are performed within a two-dimensional framework, the reported switching energy represents the optical energy absorbed inside the effective GST simulation domain. The absorbed power density Q is integrated over the GST cross-sectional area and simulation time while assuming a unit out-of-plane thickness. Therefore, the reported 4 pJ represents the absorbed energy within the effective GST simulation domain rather than the launched pulse energy.

Consequently, the reported switching energy (~4 pJ) corresponds to the effective absorbed energy responsible for inducing the GST phase transition rather than the launched optical pulse energy at the waveguide input. Parameters such as optical coupling efficiency, three-dimensional confinement, and total launched pulse energy are beyond the scope of the present two-dimensional model. Accordingly, all switching-energy values reported throughout this work refer exclusively to the absorbed energy within the active GST region, providing a physically consistent metric for evaluating the intrinsic thermo-plasmonic switching performance.

Transient simulations predict switching times ranging from approximately 50 to 200 ns, which are consistent with experimentally reported GST switching dynamics in plasmonic structures. The achievable switching speed is primarily limited by thermal diffusion and phase-transition kinetics of GST, establishing a practical lower bound within the tens-of-nanoseconds regime for the proposed nanoscale geometry. Previous experimental studies have demonstrated reliable cycling stability of thin GST films under comparable operating conditions [111–113], while the high thermal conductivity of the surrounding silver further facilitates heat extraction and reduces the possibility of thermal degradation.

It should be emphasized that the proposed device is designed for neuromorphic photonic applications rather than ultrafast optical modulation. Although Kerr-based nonlinear devices provide femtosecond-scale switching due to their instantaneous electronic response, they remain inherently volatile and therefore cannot retain synaptic states without continuous optical excitation [114–116]. In contrast, GST-based switching relies on thermally driven phase transitions, resulting in nanosecond-scale switching dynamics while providing intrinsic non-volatility and stable state retention. This operating timescale is fully compatible with neuromorphic computing, where synaptic update operations typically occur within the nanosecond-to-microsecond range rather than at optical carrier frequencies [117–119].

Overall, the excellent agreement between electromagnetic confinement, localized thermal response, experimentally validated GST material parameters, and the coupled multiphysics simulations confirms the physical robustness of the proposed thermo-plasmonic switching mechanism. Within the assumptions of the adopted two-dimensional simulation framework, the reported transmission contrast, absorbed switching energy, and thermal characteristics provide a reliable basis for evaluating the proposed device as a compact, energy-efficient, and non-volatile optical switching element suitable for neuromorphic photonic applications [120].

Finally, to systematically evaluate the robustness and tunability of the proposed device, a parametric study is performed by varying both the GST dimensions and the geometrical parameters of the dual-stub resonator. The effects of these variations on transmission contrast, resonance wavelength, and spectral response are presented and discussed in Figs. 7 and 8.

4. Tunability analysis of GST and resonator dimensions on optical response

To precisely evaluate the tunability of the proposed structure, the effects of the geometric dimensions of both the GST region and the stub resonators are investigated independently with respect to their influence on transmission contrast. These analyses aim to optimize key performance metrics including transmission contrast, resonance wavelength position, and spectral tunability. The reported transmission characteristics correspond to the selected operating wavelength of approximately 1800 nm, at which the maximum transmission contrast is obtained following systematic geometric optimization of the proposed device. The parametric analyses presented in this section therefore identify the structural dimensions that maximize the transmission contrast at this operating wavelength. The results are presented in Figs. 7 and 8. Importantly, the obtained optimized dimensions are also consistent with the fabrication feasibility constraints discussed in Section 5.

4.1. Effect of GST dimensions on transmission contrast

Fig. 7 illustrates the influence of GST geometrical parameters on the

Table 3
Thermophysical properties of the constituent materials used in the transient thermal simulations of the proposed thermo-plasmonic switch. The listed density (ρ), specific heat capacity (c_p), and thermal conductivity (κ) of amorphous/crystalline GST and silver (Ag) are employed in the coupled electro-thermal model to evaluate heat generation, temperature evolution, and phase-transition dynamics.

Material	Density ρ (kg/m^3)	Specific Heat cp (J/kg·K)	Thermal Conductivity κ (W/m·K)	Notes
GST (amorphous/crystalline)	~6150	~200	0.2 – 0.6 (phase-dependent)	Values assumed constant during simulations
Silver (Ag)	10490	235	~429	Representative room-temperature properties assumed constant during simulations

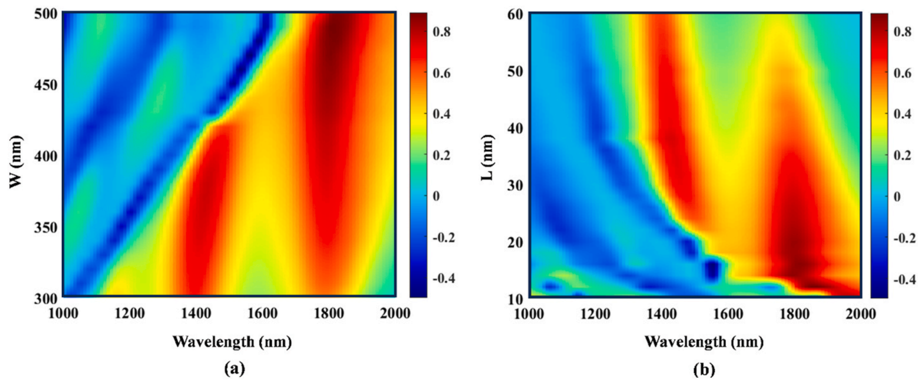

Fig. 7. Influence of GST geometrical parameters on the optical response of the proposed plasmonic switch. (a) Optical contrast as a function of GST length (15–60 nm) and wavelength (1000–2000 nm), showing that the transmission contrast increases up to an optimum GST length of approximately 35 nm before reaching saturation due to the finite extent of the localized plasmonic field. (b) Effect of GST width (10–30 nm) on the transmission response, demonstrating that narrower GST regions provide stronger electromagnetic field confinement and higher transmission contrast, whereas increasing the GST width weakens the plasmon–GST interaction and reduces the modulation efficiency. The optimized GST dimensions (35 × 10 nm^2) are selected based on these results and are used throughout the subsequent electromagnetic and thermo-optical analyses.

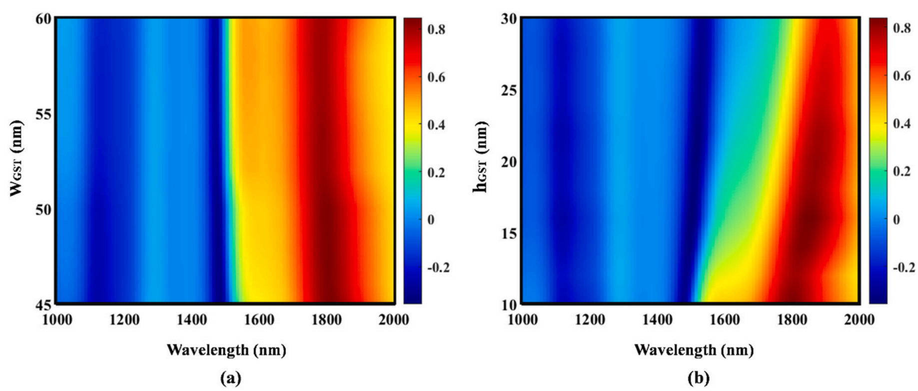

Fig. 8. Effect of dual-stub resonator geometry on the optical response of the proposed plasmonic switch. (a) Variation of the resonator length (300–500 nm) produces a systematic resonance redshift by increasing the effective optical path of the Fabry–Pérot-like cavity, thereby modifying the transmission contrast at the selected operating wavelength. (b) Influence of resonator width (10–60 nm) on the optical response, showing that narrower resonator widths provide stronger electromagnetic field confinement, enhanced plasmon–GST interaction, and higher transmission contrast, whereas wider resonators weaken mode confinement and reduce the modulation efficiency. The optimized resonator dimensions adopted in this work are selected based on these parametric results to achieve maximum transmission contrast while remaining compatible with practical nanofabrication constraints.

optical response of the device. In Fig. 7(a), the GST length is varied from 15 to 60 nm over the wavelength range of 1000–2000 nm. The results indicate that increasing the GST length enhances the transmission contrast up to an optimum value around 35 nm. This improvement arises from the increased overlap between the confined plasmonic hotspot and the phase-change region, leading to stronger modulation of absorption between amorphous and crystalline states. Beyond this optimum, saturation occurs due to the finite spatial extent of the electromagnetic hotspot. The optimum GST dimensions (35 × 10 nm^2) adopted throughout the remainder of this work are selected based on this parametric optimization, providing the highest transmission contrast while maintaining strong field localization and fabrication feasibility.

In Fig. 7(b), the effect of GST width variation (10–30 nm) is analyzed. A monotonic reduction in transmission contrast is observed with increasing GST width. This behavior is attributed to reduced field confinement and weaker overlap between the plasmonic mode and the active GST region, which decreases the sensitivity of the effective refractive index modulation induced by phase transition. The highest transmission contrast is achieved at the minimum width (10 nm), where field localization is strongest. Further reduction of the GST width is not considered because fabrication tolerances become increasingly challenging below 10 nm, while wider GST regions weaken plasmonic confinement and reduce modulation efficiency.

4.2. Effect of stub resonator dimensions on transmission performance

Fig. 8 presents the influence of the dual-stub resonator geometry on the optical response of the proposed plasmonic switch. Fig. 8(a) illustrates the effect of varying the resonator length from 300 to 500 nm. Increasing the resonator length produces a systematic redshift of the resonance wavelength, which is consistent with the Fabry–Pérot-like resonance behavior of the coupled stub cavities. As the physical cavity length increases, the effective optical path becomes longer, resulting in resonance at lower optical frequencies (longer wavelengths). The transmission contrast is simultaneously modified because the interference condition between the reflected surface plasmon polariton modes is altered by the cavity geometry. The optimized resonator length adopted in the proposed device corresponds to the geometry providing the highest transmission contrast at the selected operating wavelength and is therefore used throughout the subsequent analyses.

Fig. 8(b) shows the effect of varying the resonator width between 10 and 60 nm. Increasing the stub width produces a broader optical mode distribution inside the cavity and reduces electromagnetic field confinement within the resonant region. Consequently, the localized plasmonic hotspot becomes weaker, reducing the interaction between the confined optical field and the GST active region. This reduced coupling lowers the transmission contrast of the device. Conversely, narrower resonator widths in the range of 10–20 nm provide stronger field localization, improved resonant confinement, and enhanced optical modulation. Considering both the optical performance and practical nanofabrication constraints, the selected resonator width represents a balanced compromise between strong plasmonic confinement, high transmission contrast, and fabrication robustness.

Overall, the parametric optimization demonstrates that the optical response of the proposed plasmonic switch is predominantly governed by the combined optimization of the GST active region and the dual-stub resonator geometry. The selected structural dimensions are not arbitrary but are obtained through systematic optimization to maximize transmission contrast while preserving compactness, strong plasmonic confinement, and practical fabrication feasibility. These optimized geometrical parameters are therefore adopted consistently throughout the remainder of this work in all electromagnetic and thermo-optical simulations.

5. Fabrication considerations

Although the proposed plasmonic switch is demonstrated through full-wave numerical simulations, its geometry is designed to remain compatible with state-of-the-art nanofabrication techniques used in plasmonic and phase-change nanophotonic devices. Importantly, experimental demonstrations of GST-based nanostructures and sub-50 nm plasmonic gaps have been widely reported in the literature, confirming the feasibility of the proposed dimensional scale.

The fabrication process typically begins with the deposition of a transparent SiO_2 substrate with low surface roughness to ensure optical quality. Subsequently, a silver (Ag) layer ($\sim$50 nm) is deposited using thermal evaporation or magnetron sputtering to support low-loss surface plasmon polariton (SPP) propagation. To improve chemical stability and prevent oxidation of silver, a thin Al_2O_3 passivation layer ($\sim$5 nm) can be deposited using atomic layer deposition (ALD), which is a standard technique in plasmonic device fabrication.

The MIM waveguide and dual-stub resonator pattern are defined using high-resolution electron beam lithography (EBL) or focused ion beam (FIB) milling, both of which are routinely used for sub-20 nm plasmonic structures. In particular, EBL systems combined with optimized resist processes have demonstrated feature sizes approaching 10–20 nm, while self-aligned lithographic techniques further improve dimensional control in plasmonic nanogaps.

The GST active region (35×10 nm^2) is integrated into the hotspot using RF sputtering, pulsed laser deposition (PLD), or thermal evaporation, followed by lift-off or hard-mask patterning to achieve nanoscale placement. Although the proposed GST dimensions approach the lower limit of conventional nanolithography, comparable GST volumes and nanoscale phase-change elements have already been experimentally demonstrated in plasmonic waveguides and nanogap devices, confirming that the proposed geometry lies within current state-of-the-art fabrication capabilities.

From a practical standpoint, fabrication imperfections such as edge roughness, line-edge fluctuations, and alignment tolerances ($\pm$5–10 nm) may slightly modify the local electromagnetic field distribution, resulting in minor variations in the resonance wavelength and transmission contrast. Consequently, the optimized dimensions reported in this work represent a practical compromise between optical performance and fabrication tolerance rather than an idealized numerical optimum. Nevertheless, owing to the strong near-field confinement provided by the dual-stub configuration, the proposed device is expected to maintain robust ON/OFF switching behavior under moderate fabrication deviations. This intrinsic tolerance further enhances the reliability and practical manufacturability of the proposed design.

It is also important to note that while large-scale integration may be affected by lithographic variability and nanoscale alignment errors, the present work primarily targets proof-of-concept demonstration. Therefore, such fabrication constraints are consistent with current experimental practices in nanoscale plasmonics and phase-change photonics.

After material deposition, phase transitions in the GST layer are induced via controlled optical or thermal excitation. Electro-thermal simulations confirm that the absorbed switching energy is highly localized within the GST region, thereby minimizing thermal diffusion into the surrounding metallic and dielectric layers while preserving structural integrity. Finally, an encapsulation layer (Al_2O_3 or Si_3N_4) is applied to protect the device from oxidation and environmental degradation.

The geometrical parameters of both the GST active region and the dual-stub resonator adopted in this work are determined through systematic parametric optimization to achieve maximum transmission contrast, robust resonance behavior, and compatibility with current nanofabrication capabilities. In particular, the GST dimensions are selected to maximize electromagnetic field confinement at the plasmonic hotspot while remaining consistent with experimentally demonstrated fabrication limits for nanoscale phase-change devices.

6. Analysis and comparison of our proposed plasmonic optical switch with phase-change material (PCM) and Kerr nonlinearity-based switches

In this section, the performance of the proposed thermo-plasmonic optical switch is compared with representative optical switching devices based on phase-change materials (PCMs) and Kerr nonlinear mechanisms reported in the literature. The comparison encompasses silicon photonic, photonic crystal, and plasmonic platforms using key performance metrics including device footprint, optical transmission contrast, and switching energy. The objective is to position the proposed device within the current state of the art while highlighting its suitability for neuromorphic photonic applications.

As summarized in Table 4, PCM-based optical switches generally provide non-volatile operation together with a large refractive-index modulation, enabling Transmission contrasts typically ranging from approximately 60% to 90% while maintaining stable optical-state retention. However, many reported PCM devices employ footprints extending from tens to thousands of square micrometers and require switching energies ranging from tens to hundreds of picojoules, which may limit large-scale integration in densely interconnected neuromorphic photonic circuits.

Conversely, plasmonic switches relying on Kerr nonlinearities generally exhibit extremely compact footprints together with ultrafast femtosecond-to-picosecond response owing to their purely electronic nonlinear mechanism. Nevertheless, these devices are intrinsically volatile and therefore do not provide persistent optical memory. As a consequence, their reported transmission contrasts are typically limited to approximately 49–65%, making them less suitable for applications requiring non-volatile synaptic weight storage.

The proposed device is conceptually related to previously reported dual-stub plasmonic Kerr-based switches, particularly the 2021 design employing an Au:SiO_2 nonlinear medium [54], which achieved an optical contrast of approximately 49% within a compact plasmonic footprint. In the present work, the nonlinear Kerr medium is replaced by a nanoscale GST active region (35×10 nm^2), while the dual-stub resonator geometry is systematically optimized to maximize electromagnetic field confinement within the phase-change region. This design strategy increases the transmission contrast to more than 87% while simultaneously reducing the effective absorbed switching energy to approximately 4 pJ. In addition, the incorporation of GST introduces non-volatile operation, enabling stable synaptic-weight storage without continuous optical bias.

A comparison of the most recent entries in Table 4 further indicates a general trend toward improved optical performance through enhanced field confinement, optimized resonator geometries, and advanced phase-change materials. The proposed device follows this trend by

Table 4
Comparative performance of representative optical switches based on phase-change materials (PCMs) and Kerr nonlinear mechanisms reported in the literature. The comparison includes silicon photonic, photonic crystal, and plasmonic platforms in terms of switching mechanism, active material, device footprint, optical transmission contrast, and switching energy, highlighting the competitive performance of the proposed thermo-plasmonic GST-based dual-stub MIM switch for compact and energy-efficient neuromorphic photonic applications.

Ref	Year	Platform	Switching Mechanism	Active Material	Footprint (μm^2)	Transmission Contrast (%)	Switching Energy (pJ)
[79]	2015	Silicon	Phase-Change Material (PCM)	$SiVO_2$	10000	16	1400
[60]	2015	Plasmonic	Kerr Nonlinearity	$Au:SiO_2$	0.002	65	—
[61]	2015	Silicon	PCM	GST	1.00	21	430
[]	2017	Silicon	PCM	GST	289	27	20
[93]	2017	Silicon	PCM	GST	3600	63	190
[10]	2017	Silicon	PCM	GST	504	18	216–404
[121]	2018	Plasmonic	Kerr Nonlinearity	Ag/BaO	0.61	56	—
[63]	2018	Silicon	PCM	GST	3600	74	620
[122]	2018	Plasmonic	Kerr Nonlinearity	Ag/BaO	0.26	49	—
[91]	2019	Silicon	PCM	GSST	900	35	5.5×10^6
[29]	2019	Photonic Crystal	PCM	GST	13.80	96	150
[123]	2019	Plasmonic	Kerr Nonlinearity	Ag/BaO	0.84	64	—
[80]	2019	Plasmonic	PCM	GST	—	60	16
[84]	2019	Silicon	PCM	GST	180	78	—
[19]	2019	Silicon	PCM	GST	183600	8	430/71
[53]	2020	Plasmonic	Kerr Nonlinearity	$Au:SiO_2$	15.75	62	—
[75]	2020	Plasmonic	PCM	GST	29.22	62	—
[55]	2021	Plasmonic	Kerr Nonlinearity	$Au:SiO_2$	0.35	59	—
[99]	2021	Plasmonic	PCM	Sb_2Se_3	198	—	14000
[54]	2021	Plasmonic	Kerr Nonlinearity	$Au:SiO_2$	0.31	49	—
[70]	2022	Plasmonic	PCM	GST	—	1.50	650
This work	2026	Plasmonic (MIM dual-stub)	Thermo-plasmonic PCM switching	GST	0.035	>87	~4 (2–8 range)

Note: The switching-energy values listed in Table 4 are taken directly from the corresponding references and may represent different physical definitions, including absorbed optical energy, launched optical pulse energy, or electrical programming energy, depending on the reported experimental or simulation methodology. The value reported for the proposed device corresponds to the effective absorbed optical energy within the active GST region, as defined in Section 3.

combining strong plasmonic localization with nanoscale GST integration, thereby improving light–matter interaction and reducing the energy required for reversible phase transitions. Consequently, higher synaptic density and lower energy consumption can be achieved, both of which are highly desirable for large-scale neuromorphic photonic integration.

Overall, the comparative analysis demonstrates that the proposed thermo-plasmonic GST switch provides a favorable balance among transmission contrast, switching energy, device compactness, and non-volatility. Although Kerr-based switches remain advantageous for applications requiring ultrafast optical modulation, their lack of intrinsic memory limits their applicability in photonic synaptic systems. By contrast, the proposed device combines strong plasmonic confinement with reversible GST phase transitions, providing an energy-efficient, compact, and non-volatile optical switching platform that is well suited for programmable photonic neural networks.

7. Conclusion

In this work, a compact thermo-plasmonic optical switch based on a metal–insulator–metal (MIM) dual-stub resonator incorporating a $Ge_2Sb_2Te_5$ (GST) phase-change material is proposed and numerically investigated for neuromorphic photonic applications. Rather than relying solely on the large refractive-index contrast of GST, the proposed architecture combines systematic co-design of the dual-stub resonator with hotspot-engineered placement of the nanoscale GST element to maximize electromagnetic field confinement and strengthen light–matter interaction within the active region. This integrated design strategy enables efficient optical modulation while maintaining an ultra-compact device footprint. The optimized device geometry, particularly the reduced stub separation (~30 nm), provides strong near-field coupling and efficient resonance modulation, resulting in an overall footprint of approximately 0.035 μm^2. Numerical simulations demonstrate a transmission contrast exceeding 87% together with an effective absorbed switching energy of approximately 4 pJ within the GST active region. These results indicate that strong optical modulation can be achieved with low switching energy while preserving the non-volatile characteristics of phase-change materials. The optimized localization of the electromagnetic hotspot further improves the interaction between the confined plasmonic field and the GST region, providing an efficient mechanism for programmable optical transmission and synaptic-weight implementation. The proposed switching mechanism is governed by thermally induced reversible phase transitions in GST and therefore operates in the nanosecond regime rather than the femtosecond regime characteristic of Kerr-nonlinearity-based optical switches. However, this operating timescale is well aligned with the requirements of neuromorphic photonic systems, where non-volatile state retention, energy efficiency, and multi-level programmability are generally of greater importance than ultrafast carrier dynamics. Consequently, the inherent trade-off between switching speed and non-volatility is compensated by the functional advantages required for photonic synaptic devices. Comparative analysis with representative PCM- and Kerr-based optical switches further demonstrates that the proposed device achieves a favorable balance among compact footprint, high transmission contrast, low switching energy, and non-volatile operation. These characteristics highlight the effectiveness of combining plasmonic field confinement with nanoscale phase-change materials to improve switching performance while maintaining compatibility with practical nanophotonic integration. Overall, the present study demonstrates that hotspot-engineered GST-integrated MIM plasmonic resonators constitute a promising platform for realizing compact, energy-efficient, and programmable optical switching. The proposed architecture therefore provides a scalable building block for future neuromorphic photonic circuits requiring stable optical memory, efficient synaptic weighting, and high-density photonic integration.

Ethical statement

The authors confirm that this manuscript is original, has not been published previously, nor is it under consideration elsewhere. All authors take full responsibility for the authenticity and accuracy of the data and analyses presented, with no fabrication or unethical conduct. Additionally, no other individuals have contributed to this work in a capacity warranting authorship.

Funding statement

This study received no external funding or financial support from any organizations, institutions, or agencies.

CRediT authorship contribution statement

Ozra Sharifipour: Formal analysis, Software, Writing – original draft. **Parviz Keshavarzi:** Conceptualization, Supervision, Validation. **Mohammad Danaie:** Conceptualization, Supervision, Validation, Writing – review & editing.

Declaration of competing interest

The authors declare that they have no known competing financial interests or personal relationships that could have appeared to influence the work reported in this paper.

Data availability

All numerical data, design specifications, and supplementary materials related to this work are available and can be provided upon reasonable request by contacting the corresponding author.

References

[1] B.J. Shastri, A.N. Tait, T. Ferreira de Lima, W.H. Pernice, H. Bhaskaran, C. D. Wright, P.R. Prucnal, Photonics for artificial intelligence and neuromorphic computing, Nat. Photonics 15 (2) (2021 Feb) 102–114.
[2] D.A. Miller, Attojoule optoelectronics for low-energy information processing and communications, J. Lightwave Technol. 35 (3) (2017 Jan 4) 346–396.
[3] W. Bogaerts, D. Pérez, J. Capmany, D.A. Miller, J. Poon, D. Englund, F. Morichetti, A. Melloni, Programmable photonic circuits, Nature 586 (7828) (2020 Oct 8) 207–216.
[4] G. Indiveri, S.C. Liu, Memory and information processing in neuromorphic systems, Proc. IEEE 103 (8) (2015 Jul 15) 1379–1397.
[5] X. Meng, G. Zhang, N. Shi, G. Li, J. Azaña, J. Capmany, J. Yao, Y. Shen, W. Li, N. Zhu, M. Li, Compact optical convolution processing unit based on multimode interference, Nat. Commun. 14 (1) (2023 May 24) 3000.
[6] Y. Xiang, H. Cao, C. Liu, J. Guo, D. Dai, High-speed waveguide Ge/Si avalanche photodiode with a gain-bandwidth product of 615 GHz, Optica 9 (7) (2022 Jul 5) 762–769.
[7] W. Bogaerts, D. Pérez, J. Capmany, D.A. Miller, J. Poon, D. Englund, F. Morichetti, A. Melloni, Programmable photonic circuits, Nature 586 (7828) (2020 Oct 8) 207–216.
[8] D.A. Miller, Attojoule optoelectronics for low-energy information processing and communications, J. Lightwave Technol. 35 (3) (2017 Jan 4) 346–396.
[9] A. Tsakyridis, M. Moralis-Pegios, G. Giamougiannis, M. Kirtas, N. Passalis, A. Tefas, N. Pleros, Photonic neural networks and optics-informed deep learning fundamentals, APL Photonics 9 (1) (2024 Jan 1).
[10] Z. Cheng, C. Ríos, W.H. Pernice, C.D. Wright, H. Bhaskaran, On-chip photonic synapse, Sci. Adv. 3 (9) (2017 Sep 27) e1700160.
[11] C. Xiang, W. Jin, D. Huang, M.A. Tran, J. Guo, Y. Wan, W. Xie, G. Kurczveil, A. M. Netherton, D. Liang, H. Rong, High-performance silicon photonics using heterogeneous integration, IEEE J. Sel. Top. Quant. Electron. 28 (3) (2021 Nov 9) 1–5. Hybrid Integration for Silicon Photonics).
[12] D. Brunner, B.J. Shastri, M.A. Qadasi, H. Ballani, S. Barbay, S. Biasi, P. Bienstman, S. Bilodeau, W. Bogaerts, F. Böhm, G. Brennan, et al., Roadmap on neuromorphic photonics, arXiv preprint (2025 Jan 14) 1–239, https://doi.org/10.48550/arXiv.2501.07917, arXiv:2501.07917.
[13] G. Di Martino, S. Tappertzhofen, Optically accessible memristive devices, Nanophotonics 8 (10) (2019 Sep 25) 1579–1589.
[14] B.J. Shastri, A.N. Tait, T. Ferreira de Lima, W.H. Pernice, H. Bhaskaran, C. D. Wright, P.R. Prucnal, Photonics for artificial intelligence and neuromorphic computing, Nat. Photonics 15 (2) (2021 Feb) 102–114.
[15] Y. Zhao, X. Wang, D. Gao, J. Dong, X. Zhang, On-chip programmable pulse processor employing cascaded MZI-MRR structure, Front. Optoelectron. 12 (2) (2019 Jun) 148–156.
[16] W. Bogaerts, D. Pérez, J. Capmany, D.A. Miller, J. Poon, D. Englund, F. Morichetti, A. Melloni, Programmable photonic circuits, Nature 586 (7828) (2020 Oct 8) 207–216.
[17] C. Pappas, T. Moschos, T. Alexoudi, C. Vagionas, N. Pleros, 16-bit (4× 4) optical random access memory (RAM) bank, J. Lightwave Technol. 41 (3) (2022 Sep 12) 949–956.
[18] C. Pappas, T. Moschos, T. Alexoudi, C. Vagionas, N. Pleros, Caching with light: a 16-bit capacity optical cache memory prototype, IEEE J. Sel. Top. Quant. Electron. 29 (2) (2023 Feb 22). Optical Computing):1-1.
[19] J. Feldmann, N. Youngblood, C.D. Wright, H. Bhaskaran, W.H. Pernice, All-optical spiking neurosynaptic networks with self-learning capabilities, Nature 569 (7755) (2019 May 9) 208–214.
[20] B.J. Shastri, A.N. Tait, T. Ferreira de Lima, W.H. Pernice, H. Bhaskaran, C. D. Wright, P.R. Prucnal, Photonics for artificial intelligence and neuromorphic computing, Nat. Photonics 15 (2) (2021 Feb) 102–114.
[21] O. Sharifipoor, A. Ahmadi, An analog implementation of biologically plausible neurons using CCII building blocks, Neural Netw. 36 (2012 Dec 1) 129–135.
[22] J.H. Wijekoon, P. Dudek, Compact silicon neuron circuit with spiking and bursting behaviour, Neural Netw. 21 (2–3) (2008 Mar 1) 524–534.
[23] X. Meng, G. Zhang, N. Shi, G. Li, J. Azaña, J. Capmany, J. Yao, Y. Shen, W. Li, N. Zhu, M. Li, Compact optical convolution processing unit based on multimode interference, Nat. Commun. 14 (1) (2023 May 24) 3000.
[24] Y. Xiang, H. Cao, C. Liu, J. Guo, D. Dai, High-speed waveguide Ge/Si avalanche photodiode with a gain-bandwidth product of 615 GHz, Optica 9 (7) (2022 Jul 5) 762–769.
[25] A. Tsakyridis, M. Moralis-Pegios, G. Giamougiannis, M. Kirtas, N. Passalis, A. Tefas, N. Pleros, Photonic neural networks and optics-informed deep learning fundamentals, APL Photonics 9 (1) (2024 Jan 1).
[26] A.H. Nohoji, P. Keshavarzi, M. Danaie, High-performance all-optical photonic crystal synapse based on Mach-Zehnder interferometer and directional coupler utilizing GSST phase-change material, Results Phys. (2025 Jun 19) 108338.
[27] A.H. Nohoji, P. Keshavarzi, M. Danaie, High-performance all-optical photonic crystal synapse based on Mach-Zehnder interferometer and directional coupler utilizing GSST phase-change material, Results Phys. (2025 Jun 19) 108338.
[28] A.H. Nohoji, P. Keshavarzi, M. Danaie, A photonic crystal waveguide intersection using phase change material for optical neuromorphic synapses, Opt. Mater. 151 (2024 May 1) 115372.
[29] J. Von Keitz, J. Feldmann, N. Gruhler, C. Ríos, C.D. Wright, H. Bhaskaran, W. H. Pernice, Reconfigurable nanophotonic cavities with nonvolatile response, Acs Photonics 5 (11) (2018 Oct 15) 4644–4649.
[30] C. Lin, D. Prasad, S. Sinha, B. Cline, A.S. Helmy, Plasmonics: breaking the barriers of silicon photonics for high-performance chip-to-chip interconnects, in: In2020 IEEE International Electron Devices Meeting (IEDM), IEEE, 2020 Dec 12, 7-7.
[31] M.S. Salem, A.M. Abdelaleem, G.M. Nasr, M. Amin, Tunning the omnidirectional bandgap of nanoporous silicon using a semi-sinusoidal refractive index profile, Appl. Phys. A 130 (12) (2024 Dec) 933.
[32] R.M. Briggs, Hybrid Silicon Nanophotonic Devices: Enhancing Light Emission, Modulation, and Confinement, California Institute of Technology, 2011.
[33] J.A. Dionne, L.A. Sweatlock, M.T. Sheldon, A.P. Alivisatos, H.A. Atwater, Silicon-based plasmonics for on-chip photonics, IEEE J. Sel. Top. Quant. Electron. 16 (1) (2010 Feb 5) 295–306.
[34] Goykhman I, Desiatov B, Levy U. Silicon Plasmonics. InPlasmonics: Theory and Applications 2014 Jan 10 (pp. 149-166). Dordrecht: Springer Netherlands.
[35] S.A. Maier, Plasmonics: Fundamentals and Applications, springer, New York, 2007 May 16.
[36] A. Melikyan, L. Alloatti, A. Muslija, D. Hillerkuss, P.C. Schindler, J. Li, R. Palmer, D. Korn, S. Muehlbrandt, D. Van Thourhout, B. Chen, High-speed plasmonic phase modulators, Nat. Photonics 8 (3) (2014 Mar) 229–233.
[37] J.N. Anker, W.P. Hall, O. Lyandres, N.C. Shah, J. Zhao, R.P. Van Duyne, Biosensing with plasmonic nanosensors, Nat. Mater. 7 (6) (2008 Jun) 442–453.
[38] S. Khani, M. Danaie, P. Rezaei, All-optical plasmonic switches based on asymmetric directional couplers incorporating Bragg gratings, Plasmonics 15 (3) (2020 Jun) 869–879.
[39] M. Rahmatiyar, M. Danaie, M. Afsahi, Employment of cascaded coupled resonators for resolution enhancement in plasmonic refractive index sensors, Opt. Quant. Electron. 52 (3) (2020 Mar) 153.
[40] S. Khani, M. Danaie, P. Rezaei, Compact and low-power all-optical surface plasmon switches with isolated pump and data waveguides and a rectangular cavity containing nano-silver strips, Superlattice. Microst. 141 (2020 May 1) 106481.
[41] S.G. Shafagh, H. Kaatuzian, M. Danaie, Customized bandgap engineering in plasmonic-photonic crystal structures for advanced broadband and narrowband optical filtering, Opt. Quant. Electron. 57 (7) (2025 Jun 17) 383.
[42] M. Babaie, M. Afsahi, M. Danaie, Plasmonic metal–insulator–metal filter and refractive index sensor based on semi-rings coupled to a disk resonator, Sens. Imag. 26 (1) (2025 Jul 4) 100.
[43] O. Sharifipoor, A. Ahmadi, S. Alirezaee, M. Ahmadi, S. Erfani, True RMS-DC converter based on differential difference current conveyor, in: In2015 International Symposium on Signals, Circuits and Systems (ISSCS), IEEE, 2015 Jul 9, pp. 1–4.
[44] N. Korani, S. Mohammadi, A. Hocini, M. Danaie, A terahertz tunable plasmonic absorber based on step-shaped graphene patches for sensing applications, Plasmonics 7 (2025 May) 1–4.
[45] L. Hajshahvaladi, H. Kaatuzian, M. Danaie, Photonic crystal assisted excitation of surface plasmons: a high-resolution refractive index sensor based on a gold spiral in a photonic crystal resonator, Opt. Quant. Electron. 56 (9) (2024 Aug 18) 1417.
[46] M.R. Nickpay, M. Danaie, A. Shahzadi, Graphene-based tunable quad-band fan-shaped split-ring metamaterial absorber and refractive index sensor for THz spectrum, Micro Nanostruct. 173 (2023 Jan 1) 207473.

[47] G. Mohammadi, A.A. Orouji, M. Danaie, A high-performance and high-resolution optical refractive index sensor using a compact photonic crystal ring resonator, Sens. Imag. 25 (1) (2024 May 9) 26.
[48] N. Korani, M. Danaie, A plasmonic terahertz perfect absorber based on L-shaped graphene patches and gold rods, Appl. Phys. A 129 (11) (2023 Nov) 806.
[49] M. Danaie, L. Hajshahvaladi, E. Ghaderpanah, A single-mode tunable plasmonic sensor based on an 8-shaped resonator for cancer cell detection, Sci. Rep. 13 (1) (2023 Aug 26) 13976.
[50] E. Beiranvand, M. Danaie, M. Afsahi, An efficient coupling scheme between photonic crystal waveguides and plasmonic metal-insulator-metal waveguides, Plasmonics 20 (2) (2025 Feb) 701–708.
[51] O. Sharifipour, P. Keshavarzi, M. Danaie, Ultra-compact all-optical plasmonic switch with triangular resonator and phase-change materials for neuromorphic and advanced optical networks, Opt. Commun. 10 (2025 Jun) 132101.
[52] O. Sharifipour, P. Keshavarzi, M. Danaie, All-optical plasmonic synapse based on phase change material suitable for neuromorphic circuits, Opt. Quant. Electron. 57 (6) (2025 Jun) 1–35.
[53] H. Soleimani, A. Ahmadi, M. Bavandpour, O. Sharifipoor, A generalized analog implementation of piecewise linear neuron models using CCII building blocks, Neural Netw. 51 (2014 Mar 1) 26–38.
[54] O. Sharifipour, P. Keshavarzi, M. Danaie, Plasmonic photonic synapse with spectral bipolar weight control and ultra-low energy consumption using GST material, Results Opt. (2026 May 22) 101049.
[55] S. Khani, M. Danaie, P. Rezaei, Plasmonic all-optical metal–insulator–metal switches based on silver nano-rods, comprehensive theoretical analysis and design guidelines, J. Comput. Electron. 20 (1) (2021 Feb) 442–457.
[56] O. Sharifipour, P. Keshavarzi, M. Danaie, An ultra-compact low-power all-optical GST-based plasmonic switch for non-volatile neuromorphic synapses based on triangular cavity, Phys. Scripta 100 (8) (2025 Aug 1) 085563.
[57] K. Wang, Z. Xie, J. Ji, Y. Song, B. Zhang, Z. Wang, Novel optical Kerr switching photonic device based on nonlinear carbon material, Micromachines 14 (12) (2023 Dec 8) 2216.
[58] Z. Chai, X. Hu, F. Wang, X. Niu, J. Xie, Q. Gong, Ultrafast all-optical switching, Adv. Opt. Mater. 5 (7) (2017 Apr) 1600665.
[59] J.M. Barakat, A.S. Karar, R. Ghandour, Z.N. Gürkan, Advances in optical bistability: theory, devices, and emerging applications, Results Eng. (2025 Jun 3) 105540.
[60] H. Liu, G. Ren, Y. Gao, B. Zhu, H. Li, B. Wu, S. Jian, Ultrafast and low-power all-optical switch based on asymmetry electromagnetically induced transparency in MIM waveguide containing Kerr material, Opt. Commun. 353 (2015 Oct 15) 189–194.
[61] C.J. Ríos, et al., Integrated all-optical non-volatile memory in phase-change plasmonic resonators, Nat. Photonics 13 (8) (2019) 455–459.
[62] Y. Gutiérrez, A. Fernández-Pérez, S.A. Rosales, C. Cobianu, M. Gheorghe, M. Modreanu, J.M. Saiz, F. Moreno, M. Losurdo, Polarimetry analysis and optical contrast of Sb2S3 phase change material, Opt. Mater. Express 12 (4) (2022 Mar 16) 1531–1541.
[63] C. Wu, H. Yu, H. Li, X. Zhang, I. Takeuchi, M. Li, Low-loss integrated photonic switch using subwavelength patterned phase change material, Acs Photonics 6 (1) (2018 Dec 19) 87–92.
[64] N. Farmakidis, N. Youngblood, J.S. Lee, J. Feldmann, A. Lodi, X. Li, S. Aggarwal, W. Zhou, L. Bogani, W.H. Pernice, C.D. Wright, Electronically reconfigurable photonic switches incorporating plasmonic structures and phase change materials, Adv. Sci. 9 (20) (2022 Jul) 2200383.
[65] Y. Li, Y. Zhong, L. Xu, J. Zhang, X. Xu, H. Sun, X. Miao, Ultrafast synaptic events in a chalcogenide memristor, Sci. Rep. 3 (1) (2013 Apr 8) 1619.
[66] A. Manolis, J. Faneca, T.D. Bucio, A. Baldycheva, A. Miliou, F.Y. Gardes, N. Pleros, C. Vagionas, Non-volatile integrated photonic memory using GST phase change material on a fully etched Si3N4/SiO2 waveguide, InCLEO: Sci. Innovat. 10 (2020 May) (pp. STh3R-4). Optica Publishing Group.
[67] X. Chen, J. Lin, K. Wang, A review of silicon-based integrated optical switches, Laser Photon. Rev. 17 (4) (2023 Apr) 2200571.
[68] D. Kang, H. Heo, Y. Yang, J. Seong, H. Kim, J. Kim, J. Rho, Liquid crystal-integrated metasurfaces for an active photonic platform, Opto Electr. Adv. 7 (6) (2024 Apr 25) 230216, 1.
[69] T. Li, Y. Wang, W. Li, D. Mao, C.J. Benmore, I. Evangelista, H. Xing, Q. Li, F. Wang, G. Sivaraman, A. Janotti, Structural phase transitions between layered indium selenide for integrated photonic memory, Adv. Mater. 34 (26) (2022 Jul) 2108261.
[70] Y. Zhang, Q. Duan, X. Yan, Q. Zhang, Y. Lu, Nonvolatile multilevel adjustable optical switch based on plasmonic slot waveguide and GST segmented structure, Opt. Express 32 (9) (2024 Apr 19) 16548–16562.
[71] D. Tripathi, H.S. Vyas, S. Kumar, S.S. Panda, R. Hegde, Recent developments in Chalcogenide phase change material-based nanophotonics, Nanotechnology 34 (50) (2023 Sep 28) 502001.
[72] Y. Zhang, Q. Duan, X. Yan, Q. Zhang, Y. Lu, Nonvolatile multilevel adjustable optical switch based on plasmonic slot waveguide and GST segmented structure, Opt. Express 32 (9) (2024 Apr 19) 16548–16562.
[73] Y. Chen, et al., Nanoresonator-based Kerr optical switches in SiN, ACS Photonics 5 (4) (2018) 1344–1350.
[74] Q. Wang, et al., Phase-change plasmonic switch using GST, Nano Lett. 16 (9) (2016) 5836–5841.
[75] X. Zhou, et al., High contrast index modulation in GST for photonic applications, Nano Lett. 20 (5) (2020) 3550–3556.
[76] Zhang Y. Reconfigurable Photonics Based on Broadband low-loss Optical Phase Change Materials (Doctoral dissertation, Massachusetts Institute of Technology).
[77] H. Zhang, L. Zhou, B.M. Rahman, X. Wu, L. Lu, Y. Xu, J. Xu, J. Song, Z. Hu, L. Xu, J. Chen, Ultracompact Si-GST hybrid waveguides for nonvolatile light wave manipulation, IEEE Photon. J. 10 (1) (2017 Dec 13), 1-0.
[78] C. Song, Y. Gao, G. Wang, Y. Chen, P. Xu, C. Gu, Y. Shi, X. Shen, Compact nonvolatile 2×2 photonic switch based on two-mode interference, Opt. Express 30 (17) (2022) 30430–30440.
[79] C. Ríos, et al., All-photonic non-volatile multi-level memory using GST, Nat. Photonics 9 (11) (2015) 725–732.
[80] J. Feldmann, et al., Neuromorphic photonic networks based on GST, Nature 569 (7755) (2019) 208–214.
[81] F. Brückerhoff-Plückelmann, I. Bente, M. Becker, N. Vollmar, N. Farmakidis, E. Lomonte, F. Lenzini, C.D. Wright, H. Bhaskaran, M. Salinga, B. Risse, Event-driven adaptive optical neural network, Sci. Adv. 9 (42) (2023 Oct 20) eadi9127.
[82] J. Zhang, J. Zheng, P. Xu, Y. Wang, A. Majumdar, Ultra-low-power nonvolatile integrated photonic switches and modulators based on nanogap-enhanced phase-change waveguides, Opt. Express 28 (25) (2020 Nov 23) 37265–37275.
[83] A. Mahmoodi, M. Miri, M.H. Sheikhi, S.M. Pouyan, Design of high extinction ratio, low loss, and compact optical modulators and switches based on GST phase change material, J. Opt. Soc. Am. B 38 (11) (2021 Oct 6) 3261–3268.
[84] P. Xu, J. Zheng, J.K. Doylend, A. Majumdar, Low-loss and broadband nonvolatile phase-change directional coupler switches, Acs Photonics 6 (2) (2019 Jan 7) 553–557.
[85] J. Parra, J. Navarro-Arenas, M. Kovylina, P. Sanchis, Impact of GST thickness on GST-loaded silicon waveguides for optimal optical switching, Sci. Rep. 12 (1) (2022 Jun 13) 9774.
[86] C. Ríos, M. Stegmaier, P. Hosseini, D. Wang, T. Scherer, C.D. Wright, H. Bhaskaran, W.H. Pernice, Integrated all-photonic non-volatile multi-level memory, Nat. Photonics 9 (11) (2015 Nov) 725–732.
[87] J. Xia, T. Wang, Z. Wang, J. Gong, Y. Dong, R. Yang, X. Miao, Seven bit nonvolatile electrically programmable photonics based on phase-change materials for image recognition, ACS Photonics 11 (2) (2024 Jan 10) 723–730.
[88] B. Mohan, U. Boruah, R. Sonkar, N.J. Mondal, D. Chowdhury, 2D-MoX2 (X= S, Se, Te) and their nanocomposite toward sensing application: a review, Part. Part. Syst. Char. 42 (3) (2025 Mar) 2400156.
[89] M.Y. Shalaginov, S.D. Campbell, S. An, Y. Zhang, C. Ríos, E.B. Whiting, Y. Wu, L. Kang, B. Zheng, C. Fowler, H. Zhang, Design for quality: reconfigurable flat optics based on active metasurfaces, Nanophotonics 9 (11) (2020 Aug 14) 3505–3534.
[90] B.J. Shastri, A.N. Tait, T. Ferreira de Lima, W.H. Pernice, H. Bhaskaran, C. D. Wright, P.R. Prucnal, Photonics for artificial intelligence and neuromorphic computing, Nat. Photonics 15 (2) (2021 Feb) 102–114.
[91] Z. Zhang, J. Yang, W. Bai, Y. Han, X. He, J. Zhang, J. Huang, D. Chen, S. Xu, W. Xie, Chipscale plasmonic modulators and switches based on metal–insulator–metal waveguides with Ge2Sb2Te5, J. Nanophotonics 13 (4) (2019 Oct 1) 046009.
[92] Q. He, Z. Liu, Y. Lu, G. Ban, H. Tong, Y. Wang, X. Miao, Low-loss ultrafast and nonvolatile all-optical switch enabled by all-dielectric phase change materials, iScience 25 (6) (2022 Jun 17).
[93] M. Stegmaier, C. Ríos, H. Bhaskaran, C.D. Wright, W.H. Pernice, Nonvolatile all-optical 1× 2 switch for chipscale photonic networks, Adv. Opt. Mater. 5 (1) (2017 Jan) 1600346.
[94] Z. Xu, C. Chen, Z. Wang, K. Wu, H. Chong, H. Ye, Optical constants acquisition and phase change properties of Ge 2 Sb 2 Te 5 thin films based on spectroscopy, RSC Adv. 8 (37) (2018) 21040–21046.
[95] Y.X. Hou, Y. Li, Z.C. Zhang, J.Q. Li, D.H. Qi, X.D. Chen, J.J. Wang, B.W. Yao, M. X. Yu, T.B. Lu, J. Zhang, Large-scale and flexible optical synapses for neuromorphic computing and integrated visible information sensing memory processing, ACS Nano 15 (1) (2020 Dec 29) 1497–1508.
[96] E.S. Cho, S.Y. Lee, Propagation-invariant space–time plasmonic pulse in subwavelength MIM waveguide, Nanomaterials 14 (5) (2024 Feb 26) 425.
[97] D. Wu, X. Yang, N. Wang, L. Lu, J. Chen, L. Zhou, B.A. Rahman, Resonant multilevel optical switching with phase change material GST, Nanophotonics 11 (15) (2022 Aug 2) 3437–3446.
[98] H. Zhang, L. Zhou, B.M. Rahman, X. Wu, L. Lu, Y. Xu, J. Xu, J. Song, Z. Hu, L. Xu, J. Chen, Ultracompact Si-GST hybrid waveguides for nonvolatile light wave manipulation, IEEE Photon. J. 10 (1) (2017 Dec 13), 1-0.
[99] M. Delaney, I. Zeimpekis, D. Lawson, D.W. Hewak, O.L. Muskens, A new family of ultralow loss reversible phase-change materials for photonic integrated circuits: Sb2S3 and Sb2Se3, Adv. Funct. Mater. 30 (36) (2020 Sep) 2002447.
[100] C. Ríos, Q. Du, Y. Zhang, C.C. Popescu, M.Y. Shalaginov, P. Miller, C. Roberts, M. Kang, K.A. Richardson, T. Gu, S.A. Vitale, Ultra-compact nonvolatile phase shifter based on electrically reprogrammable transparent phase change materials, PhotoniX 3 (1) (2022 Oct 26) 26.
[101] R. Chen, Z. Fang, C. Perez, F. Miller, K. Kumari, A. Saxena, J. Zheng, S.J. Geiger, K.E. Goodson, A. Majumdar, Non-volatile electrically programmable integrated photonics with a 5-bit operation, Nat. Commun. 14 (1) (2023 Jun 12) 3465.
[102] Dao KP. Modeling Compact Non-volatile Photonic Switching Based on Optical Phase Change Material and Graphene Heater (Doctoral dissertation, Massachusetts Institute of Technology).
[103] H. Zhang, L. Zhou, L. Lu, J. Xu, N. Wang, H. Hu, B.A. Rahman, Z. Zhou, J. Chen, Miniature multilevel optical memristive switch using phase change material, Acs Photonics 6 (9) (2019 Aug 22) 2205–2212.
[104] V.V. Ionin, A.V. Kiselev, A.A. Burtsev, V.A. Mikhalevsky, N.N. Eliseev, I. M. Asharchuk, V.I. Sokolov, A.A. Lotin, An optical synapse based on a polymer waveguide with a GST225 active layer, Appl. Phys. Lett. 119 (8) (2021 Aug 23).

[105] M. Wuttig, H. Bhaskaran, T. Taubner, Phase-change materials for non-volatile photonic applications, Nat. Photonics 11 (8) (2017 Aug 1) 465–476.
[106] P. Li, Y. Zhang, Y. Wang, Nonvolatile plasmonics based on optically reprogrammable phase change materials, Adv. Opt. Mater. 11 (2) (2023) 2101234.
[107] M. Stegmaier, C. Ríos, H. Bhaskaran, C.D. Wright, W.H. Pernice, Nonvolatile all-optical 1× 2 switch for chipscale photonic networks, Adv. Opt. Mater. 5 (1) (2017 Jan) 1600346.
[108] M. Zhu, S. Abdollahramezani, C. Li, T. Fan, H. Harutyunyan, A. Adibi, Dynamically tunable second-harmonic generation using hybrid nanostructures incorporating phase-change chalcogenides, Nanophotonics 11 (11) (2022 May 17) 2727–2735.
[109] Y.X. Hou, Y. Li, Z.C. Zhang, J.Q. Li, D.H. Qi, X.D. Chen, J.J. Wang, B.W. Yao, M. X. Yu, T.B. Lu, J. Zhang, Large-scale and flexible optical synapses for neuromorphic computing and integrated visible information sensing memory processing, ACS Nano 15 (1) (2020 Dec 29) 1497–1508.
[110] X. Yan, Y. Lu, Improved optical contrast of plasmonic phase change memory using a Fabry-Perot cavity, Opt. Express 32 (10) (2024 May 2) 18224–18236.
[111] S. Abdollahramezani, O. Hemmatyar, M. Taghinejad, H. Taghinejad, A. Krasnok, A.A. Eftekhar, C. Teichrib, S. Deshmukh, M.A. El-Sayed, E. Pop, M. Wuttig, Electrically driven reprogrammable phase-change metasurface reaching 80% efficiency, Nat. Commun. 13 (1) (2022 Mar 30) 1696.
[112] Q. He, Z. Liu, Y. Lu, G. Ban, H. Tong, Y. Wang, X. Miao, Low-loss ultrafast and nonvolatile all-optical switch enabled by all-dielectric phase change materials, iScience 25 (6) (2022 Jun 17).
[113] J.R. Erickson, N.A. Nobile, D. Vaz, G. Vinod, C.A. Ríos Ocampo, Y. Zhang, J. Hu, S.A. Vitale, F. Xiong, N. Youngblood, Comparing the thermal performance and endurance of resistive and PIN silicon microheaters for phase-change photonic applications, Opt. Mater. Express 13 (6) (2023 May 17) 1677–1688.
[114] W. Zhou, N. Farmakidis, J. Feldmann, X. Li, J. Tan, Y. He, C.D. Wright, W. H. Pernice, H. Bhaskaran, Phase-change materials for energy-efficient photonic memory and computing, MRS Bull. 47 (5) (2022 May) 502–510.
[115] C. Ríos, Y. Zhang, M.Y. Shalaginov, S. Deckoff-Jones, H. Wang, S. An, H. Zhang, M. Kang, K.A. Richardson, C. Roberts, J.B. Chou, Multi-level electro-thermal switching of optical phase-change materials using graphene, Adv. Photon. Res. 2 (1) (2021 Jan) 2000034.
[116] S. Abdollahramezani, O. Hemmatyar, H. Taghinejad, A. Krasnok, Y. Kiarashinejad, M. Zandehshahvar, A. Alù, A. Adibi, Tunable nanophotonics enabled by chalcogenide phase-change materials, Nanophotonics 9 (5) (2020 May 26) 1189–1241.
[117] E. Gemo, J. Faneca, S. G-C Carrillo, A. Baldycheva, W.H. Pernice, H. Bhaskaran, C. D. Wright, A plasmonically enhanced route to faster and more energy-efficient phase-change integrated photonic memory and computing devices, J. Appl. Phys. 129 (11) (2021 Mar 21).
[118] R.R. Ghosh, A. Dhawan, Integrated non-volatile plasmonic switches based on phase-change-materials and their application to plasmonic logic circuits, Sci. Rep. 11 (1) (2021 Sep 22) 18811.
[119] A. Ahmadivand, B. Gerislioglu, R. Sinha, M. Karabiyik, N. Pala, Optical switching using transition from dipolar to charge transfer plasmon modes in Ge2Sb2Te5 bridged metallodielectric dimers, Sci. Rep. 7 (1) (2017 Feb 16) 42807.
[120] N. Farmakidis, N. Youngblood, X. Li, J. Tan, J.L. Swett, Z. Cheng, C.D. Wright, W. H. Pernice, H. Bhaskaran, Plasmonic nanogap enhanced phase-change devices with dual electrical-optical functionality, Sci. Adv. 5 (11) (2019 Nov 29) eaaw2687.
[121] T. Nurmohammadi, K. Abbasian, R. Yadipour, Ultra-fast all-optical plasmonic switching in near infra-red spectrum using a Kerr nonlinear ring resonator, Opt. Commun. 410 (2018 Mar 1) 142–147.
[122] Z. Zhang, J. Yang, X. He, Y. Han, J. Zhang, J. Huang, D. Chen, S. Xu, All-optical multi-channel switching at telecommunication wavelengths based on tunable plasmon-induced transparency, Opt. Commun. 425 (2018 Oct 15) 196–203.
[123] S. Khani, M. Danaie, P. Rezaei, All-optical plasmonic switches based on asymmetric directional couplers incorporating Bragg gratings, Plasmonics 15 (3) (2020 Jun) 869–879.